Challenges in modeling unstable two-phase flow experiments in porous micromodels

Andrea Ferrari, Joachin Jimenez-Martinez, Tanguy Le Borgne, Yves Méheust, Ivan Lunati

AGU PUBLICATIONS

Water Resources Research

RESEARCH ARTICLE
10.1002/2014WR016384

Challenges in modeling unstable two-phase flow experiments in porous micromodels

Andrea Ferrari[1], Joaquin Jimenez-Martinez[2], Tanguy Le Borgne[2], Yves Méheust[2], and Ivan Lunati[1]

[1]Institute of Earth Sciences, University of Lausanne, Lausanne, Switzerland, [2]Geosciences Rennes (UMR CNRS 6118), Université Rennes 1, Rennes, France

Key Points:
- We validate our numerical approach by comparison with drainage experiments
- We demonstrate the impact of three main sources of error
- We compare the results in a deterministic and in a statistical sense

Correspondence to:
A. Ferrari,
andrea.ferrari@unil.ch

Citation:
Ferrari, A., J. Jimenez-Martinez, T. L. Borgne, Y. Méheust, and I. Lunati (2015), Challenges in modeling unstable two-phase flow experiments in porous micromodels, *Water Resour. Res.*, *51*, doi:10.1002/2014WR016384.

Received 11 SEP 2014
Accepted 6 JAN 2015
Accepted article online 14 JAN 2015

Abstract The simulation of unstable invasion patterns in porous media flow is very challenging because small perturbations are amplified, so that slight differences in geometry or initial conditions result in significantly different invasion structures at later times. We present a detailed comparison of pore-scale simulations and experiments for unstable primary drainage in porous micromodels. The porous media consist of Hele-Shaw cells containing cylindrical obstacles. By means of soft lithography, we have constructed two experimental flow cells, with different degrees of heterogeneity in the grain size distribution. As the defending (wetting) fluid is the most viscous, the interface is destabilized by viscous forces, which promote the formation of preferential flow paths in the form of a branched finger structure. We model the experiments by solving the Navier-Stokes equations for mass and momentum conservation in the discretized pore space and employ the Volume of Fluid (VOF) method to track the evolution of the interface. We test different numerical models (a 2-D vertical integrated model and a full-3-D model) and different initial conditions, studying their impact on the simulated spatial distributions of the fluid phases. To assess the ability of the numerical model to reproduce unstable displacement, we compare several statistical and deterministic indicators. We demonstrate the impact of three main sources of error: (i) the uncertainty on the pore space geometry, (ii) the fact that the initial phase configuration cannot be known with an arbitrarily small accuracy, and (iii) three-dimensional effects. Although the unstable nature of the flow regime leads to different invasion structures due to small discrepancies between the experimental setup and the numerical model, a pore-by-pore comparison shows an overall satisfactory match between simulations and experiments. Moreover, all statistical indicators used to characterize the invasion structures are in excellent agreement. This validates the modeling approach, which can be used to complement experimental observations with information about quantities that are difficult or impossible to measure, such as the pressure and velocity fields in the two fluid phases.

1. Introduction

In the last decade, increasing attention has been focused on modeling multiphase flow at the pore scale. Indeed, it is generally accepted that the extended Darcy formulation, which is traditionally used to describe multiphase flow in porous media at the continuum scale, is applicable only under specific assumptions, which are not justified in many modern applications involving complex flow regimes. This has led the research community to reconsider the problem from the fundamentals, focusing on the scale at which the physical processes occur, in order to assess the accuracy of standard Darcy models. Numerical simulations of pore-scale processes provide tools that can help to define and parameterize macroscopic quantities so that they correctly account for pore-scale heterogeneity [*Kang et al.*, 2007].

The growing interest in pore-scale modeling has been fostered by two factors: the availability of new methods to characterize the pore space with a high level of details, and the recent advances in high-performance computing. Methods such as X-ray microtomography techniques (see *Wildenschild and Sheppard* [2013] for a complete review on the subject) or magnetic resonance imaging (MRI) [see, e.g., *Yang et al.*, 2013; *Chen and Kinzelbach*, 2002; *Chen et al.*, 2002] allow reconstructing a three-dimensional porous medium from a series of two-dimensional images taken at different angles, with a resolution sufficient to identify individual grains and interfaces. This information can be used in an appropriate pore-scale model to compute the flow velocity in the pore space [*Porter et al.*, 2009; *Raeini et al.*, 2014]. Although pore-network models have been widely used due to their computational efficiency, recent advances in computational facilities have provided the resources to use methods that allow subpore resolution and are based on

conservation principles (e.g., Smoothed Particles Hydrodynamics methods (SPH), Lattice Boltzmann methods (LB), and Direct Numerical Simulation methods (DNS)). Moreover, the development of refined numerical techniques such as high-performance iterative solvers, multiscale methods, and parallel computing will enable the use of pore-scale models on domains of sizes that would have been considered intractable only a few years ago [*Ferrari and Lunati*, 2013; *Tomin and Lunati*, 2013; *Yang et al*., 2013].

Despite these advances, a compromise between numerical accuracy and domain size is still necessary when dealing with a large number of pores as encountered in porous media applications. For large and complex geometries high resolutions cannot be achieved without drastically increasing the computational costs; therefore, it becomes necessary to investigate the ability of these numerical approaches to model experimental data with a practicable resolution. In this context, a major challenge is modeling unstable flow, as it can arise, for instance, from a viscosity difference that causes the formation of preferential flow paths.

In this paper, we report on our experience in modeling experiments of unstable primary drainage in micromodels. We focus on a quasi two-dimensional (2-D) geometry consisting of a Hele-Shaw cell that contains cylindrical obstacles. Primary drainage or imbibition in quasi two-dimensional porous media has been studied since the pioneering works performed in the 1980s, either in network channels [*Lenormand and Zarcone*, 1985; *Lenormand et al*., 1988] or in monolayers of beads [*Måløy et al*., 1985, 1987; *Méheust et al*., 2002]. During drainage, the defending fluid wets the solid walls, so that capillary forces oppose the displacement of the interface (a review article on drainage processes in two-dimensional systems was written by *Toussaint et al*. [2012]). When the defending fluid is the most viscous, viscous forces destabilize the interface according to a mechanism first discovered by Saffman and Taylor in a classic Hele-Shaw cell [*Saffman and Taylor*, 1958]. In quasi two-dimensional porous media, the presence of obstacles causes capillary forces to act at the scale of the pore necks, which leads to different displacement structures depending on the relative magnitude of viscous to capillary forces, which is quantified by the capillary number. The limiting configurations for low and high capillary numbers are capillary fingering and viscous fingering, respectively; they have been first classified in Lenormand's phase diagram [*Lenormand et al*., 1988]. More recently, it has been shown that at intermediate regimes, capillary fingering is dominant at smaller scales, while viscous fingering dominates at larger scales [*Løvoll et al*., 2004; *Toussaint et al*., 2005].

The experiments described in this paper have been performed in porous micromodels consisting of cylindrical obstacles in Hele-Shaw cells, which we have manufactured by soft lithography [*de Anna et al*., 2014]. In comparison to 3-D experiments, these quasi 2-D micromodels provide an immediate visualization of the interface dynamics through standard image acquisition techniques and make it easier to compare experiments and simulations. To model the pore-scale processes, we use Direct Numerical Simulations (DNS) of two-phase flow, in which a Navier-Stokes solver is coupled with the Volume of Fluid (VOF) method [*Hirt and Nichols*, 1981], which is used to track the interface between the two fluids. VOF is based on first principles (mass and momentum conservation) and has proved able to model drop impact onto a liquid layer [*Berberović et al*., 2009], breakup of a 3-D liquid jet in ambient air [*Gomaa et al*., 2011], wetting phenomena [*Afkhami et al*., 2009; *Lunati and Or*, 2009], and transition from stable displacement to viscous fingering in porous media [*Ferrari and Lunati*, 2013].

Our objective is to give a detailed assessment of the accuracy and limitations of modeling unstable primary drainage experiments. We compare the spatial distribution of the two fluids at breakthrough to the results of VOF simulations. In particular, we compare several macroscopic quantities such as the finger width, the fractal dimension of the interface, the length of the water-air interface in the midplane of the Hele-Shaw cell, the longitudinal saturation profile, and a measure of the mismatch between the numerical and experimental displacement structures at breakthrough. Although the experimental micromodel can be seen as a (quasi) two-dimensional medium, the constraint imposed on the flow by the presence of the bottom and top plates must be taken into account [*Hele-Shaw*, 1898]. We consider two models that account for this effect: a full-3-D model and a 2-D integrated model (similar to the one used in *Horgue et al*. [2013]), which allows saving computational time. In section 2 we present the soft lithography technique and the experimental setup, in section 3 the numerical model is described in details, while the comparison between simulations and laboratory experiments is presented in section 4 and discussed in section 5. The last section addresses conclusions and future outlooks.

2. Drainage Experiments in Micromodels

2.1. Analogous Two-Dimensional Porous Media

The experimental setup used in this work is similar to the one used by *de Anna et al*. [2014]. A two-dimensional (2-D) porous medium, consisting of a Hele-Shaw cell filled with cylindrical grains, is built using soft lithography, which is a technique commonly used in microfluidics [*Xia and Whitesides*, 1998]. A mask with the negative image of the chosen geometry is printed at high resolution and placed on top of two glass plates, between which an hydrophilic [*Wägli et al*., 2011] UV-sensitive glue is injected. Using a UV-light source, grains are polymerized at locations corresponding to the transparent regions in the mask; the glue that remains in the space between obstacles is then cleaned out using water and solvents (80% ethanol-20% acetone). The final model dimensions are $L \times W = 150$ mm $\times 90$ mm, with a thickness $a = 0.5$ mm. The mean grain diameter and the mean pore size, as well as the porosity and the absolute permeability, calculated from single-phase flow simulations are given in Table 1 for the two geometries used in the experiments. The micromodel is drained by connecting a syringe pump to the outlet, while the inlet is in contact with the atmosphere. On both sides, a triangular-shaped channel is used to connect the porous medium to the tubing in order to produce a velocity profile that is quasihomogeneous in the direction transverse to flow (see Figure 1).

The wetting fluid is a solution of *water* dyed with fluorescein (*fluorescein sodium salt*) at concentration $c = 51$ mg L^{-1}, which is used to distinguish between the wetting and nonwetting phase (*air*). The model is illuminated from below with a panel source (*backlight panel-Kesetexas*, cold cathode) that produces a light of spatially homogenous intensity. An optical filter (*LEE 126 Mauve*) is located between the light panel and the micromodel to block wavelengths in the range 505–580 nm, which allows exciting the fluorescent tracer at 494 nm (the excitation wavelength of fluorescein). A band-pass filter (*Edmunds optics*) of wavelength 521 ± 10 nm (the emission wavelength of fluorescein) is located between the model and the camera and allows only photons emitted by the solution to reach the camera (Figure 1). A CCD camera (*Princeton Instruments-Megaplus EP 11000*, actively cooled) is placed above the micromodel at a distance of 32 cm and acquires gray-scale (eight bits) images of the model, taken at regular time intervals (every 1.5 s). The images consist of 3655×2241 pixels, which corresponds to a spatial resolution of $\sim$0.04 mm per pixel (or $\sim$25 pixels per mm).

The porous medium is initially saturated with the wetting phase. The displacement is imposed by extracting the wetting phase in order to avoid compressibility effects in the gaseous nonwetting phase (*air*). A controlled flow rate $Q = 1000$ mL h^{-1} is imposed at the outlet by means of a syringe pump (*Kd Scientific* KDS210) and a glass syringe of volume 50 mL (*Tomopal Inc*.). Volumetric flow rate variations were monitored during the experiment and did not exceed 3%.

2.2. Flow Conditions

The experiments are performed at room temperature ($19 \pm 1C^{\circ}$). Under this conditions, the *water* has a viscosity around $\mu_w = 10^{-3}$ Kg m^{-1} s^{-1} and a density $\rho_w = 10^3$ Kg m^{-3}, whereas *air* has a viscosity $\mu_{nw} = 1.8 \cdot 10^{-5}$ Kg m^{-1} s^{-1} and a density $\rho_{nw} = 1.2$ Kg m^{-3}. The resulting viscosity and density ratios are $M = \mu_{nw}/\mu_w \sim 10^{-2}$ and $H = \rho_{nw}/\rho_w \sim 10^{-3}$, respectively, and the surface tension between the two fluids is $\sigma = 7.2 \times 10^{-2}$ N m^{-1}.

In addition to density and viscosity ratios, the flow regime is controlled by two more dimensionless numbers. The Reynolds number $Re = \rho_w U r/\mu_w$ (where $U = Q/Wa$ is the average flow velocity and r is the average pore size) quantifies the relative magnitude of inertial to viscous forces, whereas the capillary number $Ca = \mu U/\sigma$ quantifies the relative magnitude of viscous to capillary forces during the displacement.

In the configuration considered here, the flow is horizontal, with no significant gravity influence and the effect of the density ratio is negligible. The viscosity ratio, however, plays an important role in deciding the flow/displacement regime. In the present experiment $M < 1$ and the flow is unstable with respect to viscous forces. This is one of the most challenging regimes to simulate.

Table 1. Properties of the Two Porous Media

Property	Homogeneous	Heterogeneous
Dimensions (mm^3)	$90 \times 150 \times 0.5$	$90 \times 150 \times 0.5$
Number of grains	4536	4522
Mean radius, r (mm)	0.48	0.42
Standard deviation, Δr (mm)	0.04	0.14
Porosity, Φ (−)	75%	78%
Permeability, k (m^2)	4.32×10^{-9}	4.82×10^{-9}

3. Numerical Model

3.1. Pore-Scale Simulation Methods and Their Validations

Several methods exist to model multiphase flow at the pore scale. They can be classified into two

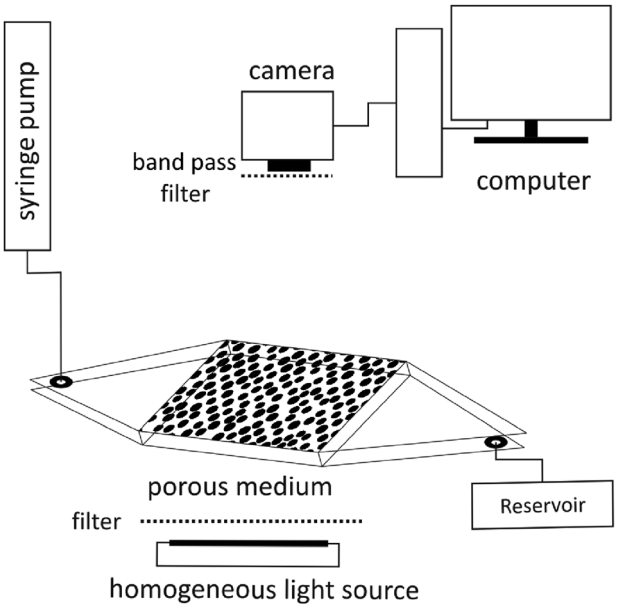

Figure 1. Scheme of the experimental setup. To perform drainage tests, the porous medium is initially saturated by the wetting phase (*dyed water*), and the wetting phase is subsequently pumped out from the outlet end of the cell, allowing the nonwetting phase (*air*) to invade the medium. A spatially homogeneous radiation of light excites the fluorescent tracer transported within the pores. A combination of optical filters allows to remove all undesirable wavelengths for excitation and emission of the fluorescent tracer.

groups: direct simulations, in which the flow equations are directly solved on a discretized pore space extracted from images of rock samples or from analogical samples; and network modeling, in which simplified flow equations are solved in an idealized pore-network derived from the real geometry [*Blunt et al*., 2013].

Since the first pioneering work [*Fatt*, 1956], pore-network models have been largely used to investigate pore-scale processes. The comparison between quasi-static pore-network models and experiments shows that they can predict relative permeability curves for two-phase flow [*Blunt et al*., 2002], three-phase flow [*Lerdahl et al*., 2000], as well as interfacial area-saturation curves [*Joekar Niasar et al*., 2009]. However, these models employ an idealization of the porous medium, which is replaced by a lattice of connected pore bodies and pore throats, and a simplified physics. Pore invasion is controlled by a certain number of filling rules that often rely on quasi-static considerations. Although some pore-network models are able to account for dynamic effects [*Aker et al*., 1998] and reproduce some features of the displacement structures (e.g., fractal dimensions, distributions of the sizes of trapped clusters) at large capillary numbers [*Aker et al*., 2000a, 2000b], their validity for benchmarking conceptual and theoretical models is always limited by the assumptions introduced in their design [*Ferrari and Lunati*, 2013]. Despite these limitations, they are attractive due to their computational efficiency. However, the continuous progress of computational facilities over the last years has made it possible to use methods that explicitly resolve the pore geometry and the interface between fluids. Since many processes, such as reactive transport or multiphase flow, have been found to strongly depend on small-scale heterogeneities, these models provide new insights to devise more appropriate macroscopic models and constitutive relationships. Several methods have been developed and successfully used to simulate two-phase flow at the pore scale; here, we briefly mention some of them and refer to *Meakin and Tartakovsky* [2009] for a complete review.

One of the most commonly used approach is the Lattice Boltzmann (LB) method, in which particles move and collide on a discrete lattice in such a way that the average motion of a large number of particles mimics the solution of the Navier-Stokes equations [*Shan and Chen*, 1993; *He and Luo*, 1997]. Viscosity, surface tension, and contact angle are modeled by means of special forces between the lattice nodes. LB methods are easier to implement than traditional CFD methods and may not require any interface tracking algorithm. The main drawbacks are the stochastic nature of the model, which requires averaging over quite a large number of particles to obtain an accurate description of the fluid flow, and the ambiguity in the relationships between internode forces and physical parameters [*Meakin and Tartakovsky*, 2009]. Moreover, numerical instabilities arise in multiphase flow simulations, limiting the range of viscosity and density ratios that can be modeled. LB methods have been used to reproduce experiments: *Porter et al*. [2009] found a good agreement between interfacial areas calculated in column-scale experiment and LB simulations during drainage, but they observed more discrepancies during imbibition; *Vogel et al*. [2005] simulated pressure-saturation curves using a full morphology model, a pore-network model and a LB model and found good correspondence among the three; *Schaap et al*. [2007]

applied a multiphase LB model to simulate the flow through a geometry obtained from microtomographic data, and found an encouraging agreement between observed and simulated water-air pressure-saturation characteristic, but less satisfactory results for a water-Sotrol system.

The Smoothed Particle Hydrodynamic method (SPH) is a fully Lagrangian particle method, which has many advantages for modeling multiphase flow in porous media [*Monaghan*, 1994; *Bandara et al*., 2011]. In particular, SPH does not require complex interface tracking schemes and it is free of numerical dispersion. Similar to LB models, fluid-fluid and fluid-solid interactions are accounted for by adding special forces between different particles. SPH has been used to model droplet flow through a Y-shaped fracture junction [*Tartakovsky and Meakin*, 2005] and the capillary trapping mechanism during CO_2 injection [*Bandara et al*., 2011]. An attempt to use SPH simulations to simulate experiments has been recently published [*Bandara et al*., 2013], but the comparison is only qualitative due to the much smaller domain considered in the simulations with respect to the experiments.

In contrast to the LB and SPH methods, Computational Fluid Dynamics (CFD) approaches are directly based on a discretized form of the partial differential equations of motion on a Eulerian mesh. For most applications, this approach is preferable due to the highly refined numerical schemes developed in traditional CFD and their ability to deal with large density and viscosity ratios [*Meakin and Tartakovsky*, 2009]. Despite its superior numerical efficiency and the conceptually straightforward extension of CFD to pore-scale modeling, the implementation for multiphase flow is more complex than for LB or SPH methods. A Navier-Stokes solver has to be coupled with an interface-capturing or an interface-tracking method which is used to advect the menisci. Interface capturing methods, such as Volume of Fluid (VOF), Level-Set (LS), or Phase Field, are normally preferred to interface tracking algorithms because they employ static meshes and are more appropriate to model complex interface deformations [*Ferrari and Lunati*, 2013]. In this work, we employ the VOF method, first introduced by Hirt and Nichols [*Hirt and Nichols*, 1981]. It has been used to model experiments of single and two-phase flow in porous media. *Yang et al*. [2013] compared steady state single-phase pore velocity in bead pack with magnetic resonance observations and found very similar spatial patterns; *Horgue et al*. [2013] studied the spreading of a liquid jet in a small array of cylinders and showed a good agreement with experiments; *Ferrari and Lunati* [2014] employed VOF simulations to assess the role of inertial effects during imbibition processes that exhibit rapid meniscus reconfigurations; *Ferrari and Lunati* [2013] demonstrated that the VOF method can correctly model the transition between stable displacement and viscous fingering under drainage, but no comparison with experiments was provided. The present work represents, to our knowledge, the first attempt to quantitatively compare the front morphology obtained by CFD-based numerical simulation with data from micromodel experiments containing a large number of pores ($>$4400).

3.2. Description of the Numerical Model

We consider the isothermal motion of two incompressible fluids within a solid matrix and adopt a whole-domain description of the system [*Scardovelli and Zaleski*, 1999; *Ferrari and Lunati*, 2013]. This formulation allows us to consider the two phases as a single fluid with space-dependent properties and replaces the jump condition at the interface by a force that acts only in the interface region. In contrast with a two-fluid formulation, it does not require solving a moving boundary problem, which is extremely difficult and computationally expensive. Below, we briefly introduce the equations of motion and the Volume of Fluid method, and we discuss the different models employed: the 2-D integrated model and the 3-D model. We then analyze the geometry and the different boundary and initial conditions used in the simulations.

3.2.1. Navier-Stokes Equations

In the whole-domain formulation the flow of two immiscible fluids is governed by a single set of Navier-Stokes equations, i.e.,

$$\nabla \cdot \boldsymbol{u} = 0, \tag{1}$$

which expresses the conservation of the total mass, and

$$\frac{\partial \rho \boldsymbol{u}}{\partial t} + \nabla \cdot (\rho u u) = -\nabla p + \nabla \cdot (2\mu \mathbf{E}) + \boldsymbol{f}_s, \tag{2}$$

which describes the conservation of momentum. In the above equations, $\boldsymbol{u}$ is the fluid velocity, p is the

pressure, and $\boldsymbol{E}=\frac{1}{2}(\nabla\boldsymbol{u}+\nabla\boldsymbol{u}^T)$ is the rate-of-strain tensor. The last term in equation (2) represents the surface force acting at the interface between the two fluids and is defined as

$$\boldsymbol{f}_s=\sigma\kappa\,\boldsymbol{n}\,\delta_\Gamma, \tag{3}$$

where σ is the surface tension, κ is the curvature of the interface, $\boldsymbol{n}$ is the normal to the interface, and δ_Γ is a Dirac function that is zero everywhere except at the interface. Therefore, $\boldsymbol{f}_s$ is nonzero only at the interface and describes the Laplace pressure.

3.2.2. The Volume of Fluid (VOF) Method

The volume of fluid method allows tracking the evolution of the interface according to the velocity field provided by the solution of the Navier-Stokes equations. The spatial distribution of the two phases is described using a color function (or fluid function), which is defined as

$$\alpha=\begin{cases}1 & \text{in the wetting fluid},\, w,\\ 0 & \text{in the non-wetting fluid},\, nw.\end{cases} \tag{4}$$

In equation (2), the density and the viscosity vary in space as they are functions of α, i.e.,

$$\rho=\alpha\rho_{\mathrm{w}}+(1-\alpha)\rho_{\mathrm{nw}} \quad \text{and} \quad \mu=\alpha\mu_{\mathrm{w}}+(1-\alpha)\mu_{\mathrm{nw}} \tag{5}$$

and the surface force, $\boldsymbol{f}_s$, is replaced by the corresponding volume force,

$$\boldsymbol{f}_v=\sigma\kappa\nabla\alpha, \tag{6}$$

which acts on the volume occupied by the interface, i.e., on the region where $0<\alpha<1$. It can be shown that this continuum interpretation of the surface force (Continuum Surface Force (CSF) model) [*Brackbill et al*., 1992] is exact when the thickness of the interface (h) goes to zero, i.e.,

$$\lim_{h\to 0}\boldsymbol{f}_v=\boldsymbol{f}_s. \tag{7}$$

The curvature is defined as the divergence of the unit normal to the interface, $\boldsymbol{n}$,

$$\kappa=-\nabla\cdot\boldsymbol{n}=-\nabla\cdot\left(\frac{\nabla\alpha}{\|\nabla\alpha\|}\right). \tag{8}$$

The wetting properties of the solid are described by imposing that the angle, θ, between the normal to the interface, $\boldsymbol{n}$, and the normal to the wall, $\boldsymbol{n}_s$, be the equilibrium contact angle defined by Young's law, $\sigma\cos\theta=\sigma_{\mathrm{nw}}-\sigma_{\mathrm{w}}$, where σ_{nw} and σ_{w} are the surface tension coefficients of the nonwetting fluid-solid and wetting fluid-solid interfaces, respectively. They can be interpreted as the energy cost of creating a unit area, or equivalently as the magnitude of the force per unit length that pulls the contact line; for a full discussion of the wetting equilibrium in terms of free energy and forces, including forces normal to the solid wall, see *Lunati* [2007]. This is equivalent to imposing that the normal to the interface on the wall, $\boldsymbol{n}_{\delta_\Gamma}$, be defined as

$$\boldsymbol{n}_{\delta_\Gamma}=\boldsymbol{n}_s\cos\theta+\boldsymbol{t}_s\sin\theta, \tag{9}$$

where $\boldsymbol{t}_s$ is the unit vector tangent to the solid, perpendicular to the contact line and pointing into the wetting phase.

Equations (1) and (2) allow computing the velocity field that determines the evolution of the interface through a simple advection equation. In the implementation of the VOF that is used here [*OpenFOAM*, 2011], the advection equation reads

$$\frac{\partial\alpha}{\partial t}+\nabla\cdot(\alpha\boldsymbol{u})+\nabla\cdot(\alpha(1-\alpha)\boldsymbol{u}_r)=0, \tag{10}$$

where the last term is an artificial compression term used to limit numerical diffusion ($\boldsymbol{u}_r$ is a suitable compression velocity [see, e.g., *OpenFOAM*, 2011; *Rusche*, 2003; *Ferrari and Lunati*, 2013]).

3.2.3. Two-Dimensional Integrated Model Versus 3-D Model

Despite the fact that the micromodel used in the experiment can be seen as a two-dimensional object, the effect of the flow confinement along the third-dimension has to be taken into account. A first approach

consists in directly solving the system of equations presented above (equations (1), (2), and (10)) in the 3-D geometry, with appropriate boundary conditions. A second approach, alternative to the full-3-D model, is a 2-D integrated model (as used in *Horgue et al.* [2013]) that accounts for the drag exerted by the two parallel plates of the Hele-Shaw cell and for the radius of curvature of the menisci in the vertical direction. In this work we employ both approaches: the 2-D integrated model allows us to save computational time at the expense of vertical resolution, while the full-3-D model is computationally more expensive but can account for complex 3-D effects. Below, we describe the equations that are solved in the 2-D integrated model in order to account for the vertical confinement of the flow by the horizontal walls.

The no-slip condition at the two parallel plates of the Hele-Shaw cell and its impact on the velocity field can be modeled by introducing a Darcy-like term in the momentum conservation equation, which accounts for the drag force exerted by the walls, i.e.,

$$\frac{\partial \rho \boldsymbol{u}}{\partial t} + \nabla \cdot (\rho u u) = -\nabla p + \nabla \cdot (2\mu \mathbf{E}) + \boldsymbol{f}_s - \frac{\mu}{k}\boldsymbol{u}. \tag{11}$$

Assuming that the vertical profile of the velocity is parabolic everywhere, the permeability can be approximated as $k = a^2/12$, where a is the aperture of the Hele-Shaw cell. If the radius of curvature in the vertical plane is assumed constant, it can be written as a function of the aperture. Then, the total curvature is the sum of the curvature calculated in the horizontal plane and the constant curvature in the vertical plane [*Horgue et al.*, 2013], i.e.,

$$\kappa = -\nabla \cdot \boldsymbol{n} - \frac{2}{a}\cos\theta. \tag{12}$$

Notice that this is an approximation of the real 3-D solution and that corner flow around the obstacles and wetting films are not captured by the 2-D model.

3.2.4. Computational Domain, Boundary, and Initial Conditions

The pore geometries used in the experiments and in the simulations have been generated from a two-dimensional packing of disks, obtained by deposition [*Vinningland et al.*, 2007]. A connected pore space of the desired porosity has been obtained by imposing a random compression of the obstacle radii. We have generated two geometries by varying the width of the grain-radius distribution while keeping the mean value constant. During the manufacturing of the micromodels, the cleaning procedure that removes the UV-sensitive glue in excess is particularly delicate and affects the final geometries of the micromodels, which differ from the generated (numerical) geometries. For example, the porosity of the numerical geometries was calculated to be around 70%, whereas the experimental porous media had a porosity around 75%; this suggests that the grain size of the micromodels was systematically smaller compared to the generated numerical geometries. These discrepancies led to unsatisfactory preliminary results (not shown here) when the simulations were performed using the "ideal" model geometry. Therefore, we measured the grain positions and radii distributions from experimental images of the micromodels and used these geometries as input for the flow simulations, rather than the original numerical geometries. The resulting properties of the two media, measured from experimental images, are shown in Table 1. Hereafter, we will refer to the weakly heterogeneous distribution as the *homogeneous* distribution, and to the strongly heterogeneous distribution as the *heterogeneous* distribution (see Figure 2).

The computational domain is obtained by discretization of the pore space by means of a mesh generator that creates split-hexahedrals (around the obstacles) and hexahedrals (elsewhere) from the triangulated surface geometry. An example of the resulting mesh around the obstacles can be found in *Ferrari and Lunati* [2013]. The simulations presented in this work are performed with the open-source code *OpenFOAM* [2011], in which equations (1), (2) (or equation (11)), and (10) are discretized by a finite volume method with an accuracy of first order in time and second order in space. Given the large number of pores considered, a compromise has to be found between discretization and computational costs. In order to capture the wetting film around the obstacles in the 3-D simulations, the mesh has to be refined significantly. A previous study [*Horgue et al.*, 2012] has shown that at least two grid cells per film thickness are necessary to accurately reproduce the wetting film with a diffuse interface model. For a 2-D geometry very similar to the one used in this work, *Ferrari and Lunati* [2013] have shown that a discretization with cell size $\Delta x = r/6$, where r is the mean pore radius, ensures that the difference with respect to the results obtained with a finer grid is

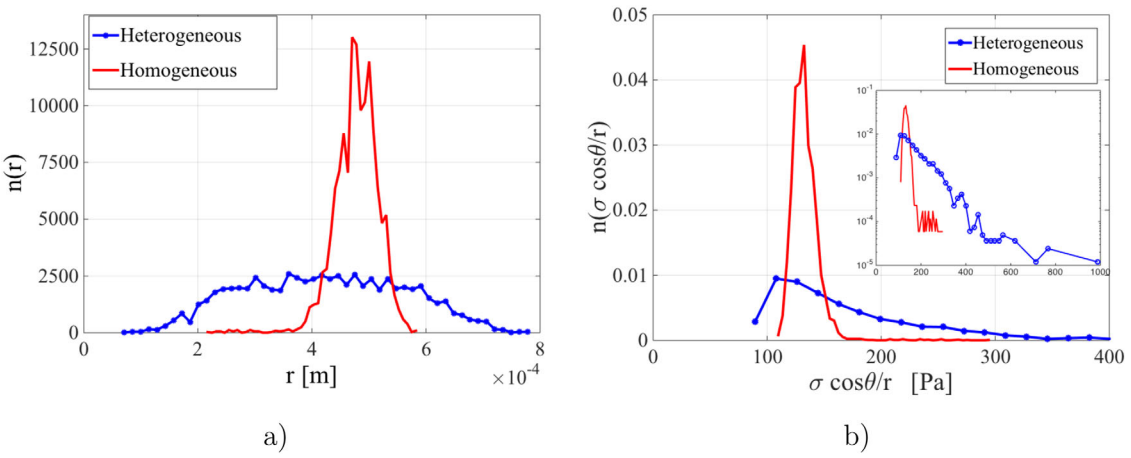

Figure 2. (a) Normalized grain radii distributions for the homogeneous (red line) and heterogeneous (blue line) geometry; (b) estimate of the normalized capillary threshold pressure distributions for the two geometries, which represents the minimum entry pressure needed to invade the various pores. It has been calculated directly for the radii distributions assuming that for each pore it is of the order of $\sigma\cos\theta/r$ (the inset shows the full range of the capillary threshold distribution in semilog scale).

below 10%. Based on these considerations, we construct the mesh with a typical cell size about 50 μm ($\Delta x \approx r/8$ for the heterogeneous geometry and $\Delta x \approx r/9$ for the homogeneous geometry), which guarantees more than two cells in the wetting film and $\Delta x < r/6$. The final mesh consists of about 4×10^6 cells for the 2-D model and 2×10^7 cells for the 3-D model; the computational time required for the 2-D simulations varies between 3 and 5 days using 80 processors, whereas about 25 days on 200 processors were required for the 3-D simulations.

No-slip boundary conditions are assigned on the solid obstacles. In the 3-D model, taking advantage of the axial symmetry of the problem, we simulate only half of the domain and assign no-slip boundary conditions on the front side (adjacent to the cell plate) and symmetry boundary conditions on midcell plane of the domain. To reproduce the experimental conditions, a constant total flux, $Q = 1000$ mL h^{-1}, is assigned at the outlet boundary, whereas a constant atmospheric pressure is specified at the inlet boundary. The equilibrium contact angles at the water-air-plate contact line as well as at the water-air-obstacles contact line are estimated from a photograph as slightly less than 30° and slightly higher than 30°, respectively. In the simulation, lacking a more accurate characterization, we set an equal equilibrium contact angle $\theta=30^\circ$ on plate and obstacles.

When dealing with unstable flow, the onset of the instability is extremely difficult to capture without an appropriate initialization. Hence, we have decided to impose two different initial conditions to study the influence of the initial configurations on the evolution of the displacement structures. The first initial condition corresponds to a medium that is fully saturated with the wetting phase (water); this corresponds to the situation at time t_0 in the experiments, when the interface has not yet entered the porous medium. As the simulation advances, water is extracted at the outlet, whereas air enters at the inlet and starts invading the porous region. The second initial condition is obtained from the first experimental image of the cell acquired after the nonwetting phase (air) has started invading the medium (i.e., the first image acquired at time $t > t_0$). We shall see that this small change in the time at which the interface position is initialized plays an important role in controlling the later evolution of the front morphology.

3.3. Flow Conditions

To reproduce the experimental conditions (see section 2.2), we used the densities and the viscosities of water as wetting fluid and air as nonwetting fluid, as well as the surface tension corresponding to this fluid pair. The Reynolds number associated with the displacement is $Re \approx 1$ for both geometries, which indicates that the flow regime is laminar [*Bear*, 1972], whereas the capillary number is $Ca \approx 8.0\times10^{-5}$ for both media. At a given volumetric flow rate, the capillary numbers for the two porous media (homogeneous and heterogeneous) are the same. What distinguishes primary drainage processes occurring in these two geometries is the ratio of the magnitude of viscous forces to that of the fluctuations in capillary pressure throughout

the medium. This is quantified by the fluctuation number [see *Méheust et al*., 2002], $F=(1/2)(r/\Delta r)Ca$, where Δr is the width of the pore size distribution. It has been conjectured [*Méheust et al*., 2002] that the fluctuation number is in turn related to the width or lateral extension, w, of the finger, $w \sim F^{-\nu/(1+\nu)}$, where ν is the correlation length; therefore, an increase in Δr results in an increase of the finger width. The fluctuation numbers for the two geometries are $F = 6\ Ca$ for the homogeneous geometry and $F = 1.5\ Ca$ for the heterogeneous one.

4. Results

In this section, the flow patterns produced by the simulations in the two geometries (homogeneous and heterogeneous) are compared with those recorded during the corresponding drainage experiments. We use two different initial conditions (with and without initialization of the finger) and two different numerical models: (i) the vertically integrated, 2-D model for both the homogeneous and the heterogeneous geometries, and (ii) the full 3-D model for the heterogeneous geometry only. Figure 3 shows the measured and the simulated displacement structures: three different times are shown for the heterogeneous geometry ($t \approx 1.5s, t \approx 3s$, and $t=t^*$, where t^* is the breakthrough time), whereas only the structure at breakthrough time is shown for the homogeneous geometry. Notice that since the injection rate is constant and we consider only times prior to the breakthrough ($t < t^*$), time and global saturation are simply related by $S_{nw}=Qt/V_{tot}$, where V_{tot} is the total pore volume of the porous medium. The saturations at breakthrough, expressed in terms of the relative difference with respect to the breakthrough saturation of the corresponding experiments, E_s, are specified in Table 2 for all simulations.

In the next sections, we will quantify the differences between the displacement structure observed in the drainage experiments and the corresponding simulations (we define the displacement structure, or invasion structure, as the portion of the cell midplane that is occupied by air). First, we compare macroscopic quantities: typical finger width, fractal dimension, air-water interfacial length, and average longitudinal saturation profile. Then, we calculate the relative mismatch area between displacement structures obtained at breakthrough (and in the midplane of the Hele-Shaw cell) by the numerical simulations and those measured in the experiments.

4.1. Typical Finger Width

The typical finger width of the structure created by air through the wetting fluid corresponds to the scale over which the viscous pressure drop in the wetting fluid starts dominating the fluctuations of the capillary pressure thresholds along the interface and dictates the shape of the displacement structure [see, e.g., *Toussaint et al*., 2005]. When it can be defined without ambiguity, the typical finger width is thus a critical feature of a two-phase flow process. However, due to the stochastic nature and the branched shape of the displacement structure, the finger width is not easy to accurately determine. We estimate the finger width by measuring the length of the transverse cuts of the structure and computing their probability density function (pdf). The pdf, which is shown in Figure 4 for the homogeneous (a) and the heterogeneous geometry (b), exhibits two main peaks, one at a length that is the mean pore size (here, about twice the mean grain radius), and the other at a length that we consider to be an estimate of the typical finger width. For the experimental displacement structures the finger width is 3.3 and 3.5 mean grain diameters (see Figure 4). The finger widths measured for the simulated structures deviate from those values by less than 10% (see Table 2).

4.2. Fractal Dimension of the Displacement Structure

The fractal dimension is a measure of the geometrical complexity of the structure and depends on the interplay between capillary and viscous forces. For very slow displacements ($Ca \ll 1$), the width of the capillary threshold distribution is larger than the viscous pressure drop over the whole system [*Løvoll et al*., 2004] and the flow is controlled by the fluctuations of capillary threshold. In this case, the displacement structure can be simply described by invasion percolation [*Lenormand and Zarcone*, 1985], which has fractal dimension $D_c=1.83\pm0.01$. At high flow rates the morphology of the front is typical of viscous fingering, which has fractal dimension $D_v \approx 1.53$ [*Toussaint et al*., 2005]. As the drainage experiments were performed at intermediate capillary numbers, we expect capillary forces to dominate at a smaller scales, while viscous forces dominate at a larger scales [*Løvoll et al*., 2004; *Toussaint et al*., 2005]. The smooth crossover between

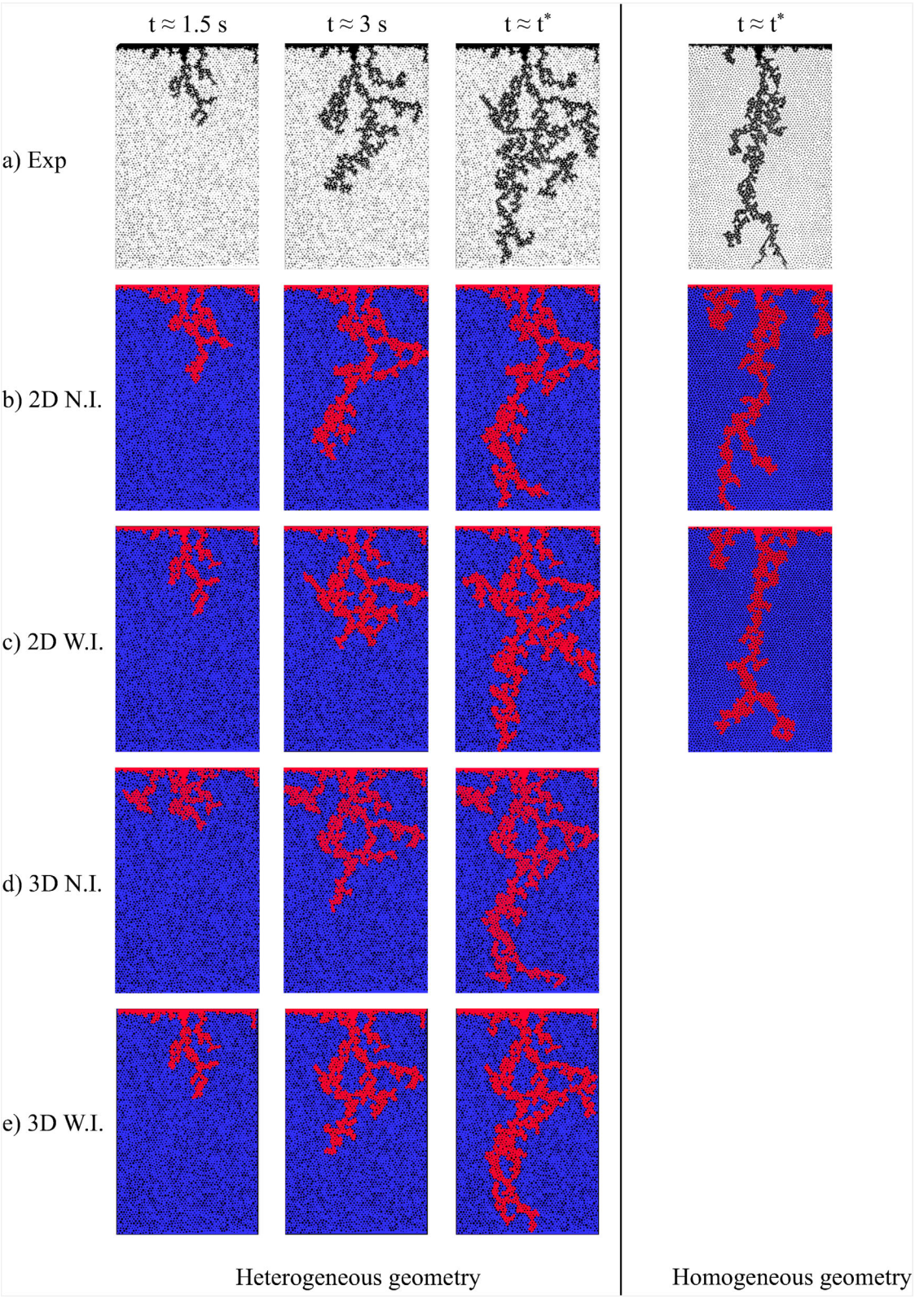

Figure 3. Experiments (first row) and simulations in the heterogeneous and homogeneous geometry for different times/saturations. t^* represents the breakthrough time; the relative differences in breakthrough times with respect to the corresponding experiment can be found as E_s in Table 2 (Exp = experiments; N.I. = simulations with no initialization; and W.I. = simulation with initialization).

Table 2. Relative Error on the Typical Finger Width, $\Delta w/w$, Saturation Errors, E_S, and Mismatch Ratio, E_{mm}, for All the Simulations in the Homogeneous and Heterogeneous Geometry (N.I. = Simulations With No Initialization and W.I. = Simulation With Initialization)

		$\Delta w/w$ (%)	$A_{exp}-A_{sim}$	E_S (%)	$\lvert A_{exp}-A_{sim}\rvert$	E_{mm} (%)
Homogeneous	2-D N.I.	−8.2	122.984	11.9	860.201	39.5
	2-D W.I.	−8.3	91.534	8.9	696.039	32.4
Heterogeneous	2-D N.I.	−3.8	362.401	21.0	883.289	28.7
	2-D W.I.	−5.7	12.182	0.7	591.397	17.2
	3-D N.I.	−6.5	190.005	11.0	802.599	24.7
	3-D W.I.	−9.8	167.411	9.7	666.351	20.3

these two regimes is expected to occur at scales close to the typical finger width, which is smaller than 3.5 mean grain diameters (see section 4.1)), so we do not expect to observe it in our data.

The fractal dimension D of the displacement structure is analyzed by the standard box-counting method. The number of boxes of size s needed to cover the displacement structure, $N(s)$, is plotted in log-log scale as function of the normalized box size s/r. The slope of the curve, which corresponds to $-D$, is calculated by linear regression of the points corresponding to the last image of the experiments and the last calculated time step of the simulation. Scales smaller than one pore diameter ($2r$) are little relevant, and in any case they should be characterized by a fractal dimension 2. At the largest scales investigated, the box size reaches the width of the system, and the fluctuations around the power law behavior increase due to the limited statistics. A meaningful fractal dimension can be calculated only in an intermediate region; therefore, we fit a power law to the data in the interval between s/r = 1 and s/r = 10–20, and find $N(s) \sim s^{-1.65\pm0.04}$ for the experiment in the homogeneous geometry and $N(s) \sim s^{-1.68\pm0.04}$ for the experiment in the heterogeneous geometry. These values are consistent with the fact that the experiments are performed at intermediate Ca. The experimental data and the numerical data are shown in Figure 5, together with the corresponding fractal dimensions, which are in good agreement between experiment and simulations.

4.3. Air-Water Interfacial Length

While it is quite easy to obtain the three interfacial areas (w – nw, w – $solid$, nw – $solid$) from the simulations [see, e.g., *Ferrari and Lunati*, 2013], no information about the third-dimension can be extracted from the 2-D experimental images and a direct measure of the experimental interfacial area is not possible. As a simple alternative, we compare the extension of the contact line between the interface and the front plate of the Hele-Shaw cell. However, this introduces an ambiguity due to the presence of wetting films in the corners formed by the plates and the obstacles: these films, which are present in the experiments, are well captured by the 3-D model, but they cannot be reproduced by the 2-D model.

To eliminate this ambiguity, we have computed the interfacial length by neglecting the wetting film on the horizontal plates, that is, by attributing the film to the air phase. This should correspond to calculating the

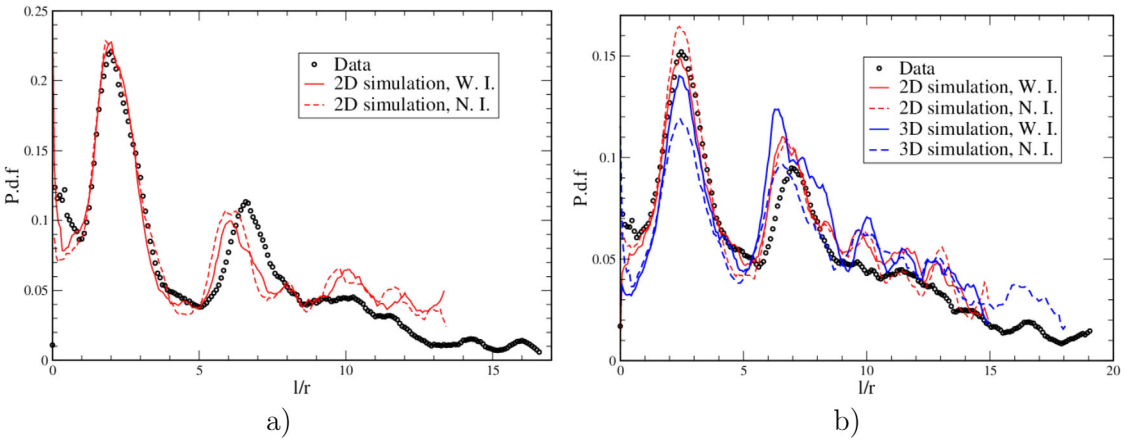

Figure 4. Probability density functions for the lengths of one-pixel-wide transverse cuts of the displacement (air) structure: (a) homogeneous medium and (b) heterogeneous medium. The peak at $2r$ indicates the mean pore size, while the second peak to its right denotes the typical finger width, of 6.6 for experimental data recorded in the homogeneous system and 7.1 for the experimental data recorded in the heterogeneous system. The corresponding relative deviations of the finger width of the simulated structures with respect to the experimental measure are shown in Table 2.

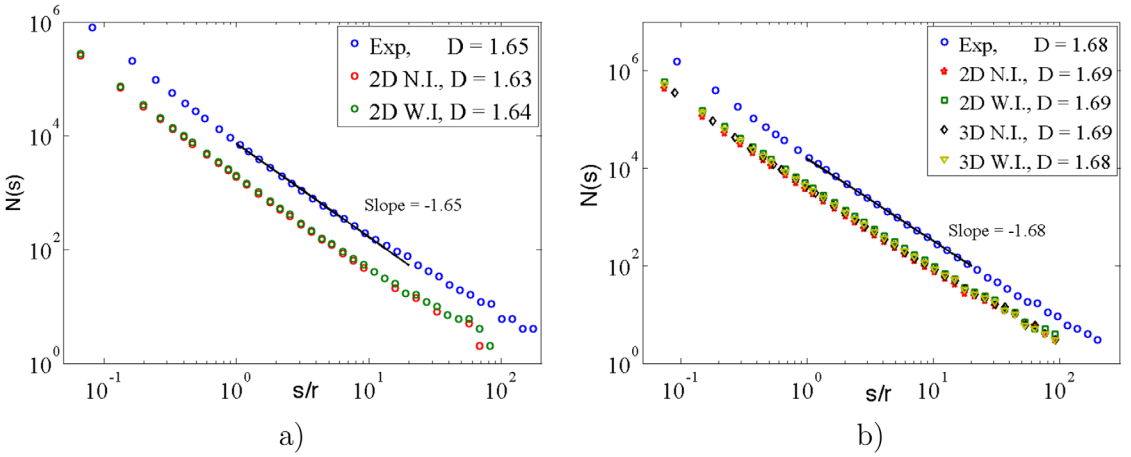

Figure 5. Fractal dimension of the invading structure at the breakthrough for experiments and simulations in (a) the homogeneous geometry and (b) the heterogeneous geometry. The slope of each curve, *D*, is calculated by linear regression of the points in the interval between s/r = 1 and s/r = 10–20, (Exp = experiments; N.I. = simulations with no initialization; and W.I. = simulation with initialization).

length of the intersection between the interface and the midcell plane. In that plane cylindrical obstacles are expected to be in contact with the air phase, because in a partial wetting regime ($\theta = 30^{\circ}$) a thin film covering the entire surface of a cylindrical grain is unstable. This hypothesis is supported by the results of the 3-D simulations, which clearly show that pendular rings exist only in the corner between the plate and the obstacles, whereas air is in direct contact with the obstacles at the midcell plane (see Figure 6g). From the raw experimental images, we isolate the films around the obstacles from the rest of the wetting phase and we attribute them to the nonwetting fluid (Figures 6a–6d). For the 3-D simulations the full information is available and the same structure can be obtained simply by extracting the color function on the midcell plane (Figures 6e–6h), which corresponds to the back plane of Figure 6g as we simulate only half a cell (see section 3.2.4). The interfacial length, L_{nw}, is then calculated by counting the pixels on the perimeter of the resulting structures for all geometries. It is plotted as a function of the saturation of the nonwetting phase in Figure 7.

4.4. Longitudinal Saturation Profiles

The interfacial length is an integrated quantity and does not provide information about fluid distributions: for the same saturation, two structures might have a very different shape while having the same interfacial length.

The typical finger width and the fractal dimension carry important information about the relevant physical processes, but they can be reliably calculated only up to a scale of 10–20 pores. They also contain little information about the penetration speed of the nonwetting phase: typical finger widths and fractal dimensions are quite similar in the two micromodels, but the saturations at breakthrough are considerably different, indicating a higher penetration speed of the air in the homogeneous geometry.

To better quantify the penetration speed, we analyze the longitudinal saturation profiles (averaged in the transverse direction) at the breakthrough time; they are plotted in Figure 8 as a function of the normalized longitudinal coordinate, Y/L. The longitudinal saturation profile is also intimately related to the traditional macroscopic description of flow through porous media, which is based on volume averaging and on the concept of Representative Elementary Volume (REV) [see, e.g., *Bear*, 1972]. In the drainage experiments, the experimental displacement structure is only poorly representative of the statistics of the invasion process due to the limited extension of the micromodels in both the longitudinal and transverse direction. However, despite the fluctuations, the longitudinal saturation profile is rather informative of the penetration speed and of the lateral extension of the displacement structures, which are different in the two geometries.

4.5. Mismatch Area

Finally, we compare the invasion structures from experiments and numerical simulations pixel by pixel, and we compute the mismatch area between them. In Figure 9, the different structures obtained at breakthrough from simulations with initialization are superimposed to the corresponding experiments to highlight differences. We denote by A_{exp} the *characteristic matrix* of the experimental displacement structure (i.e., the matrix whose values are one for pixels belonging to the displacing phase and zero otherwise) and

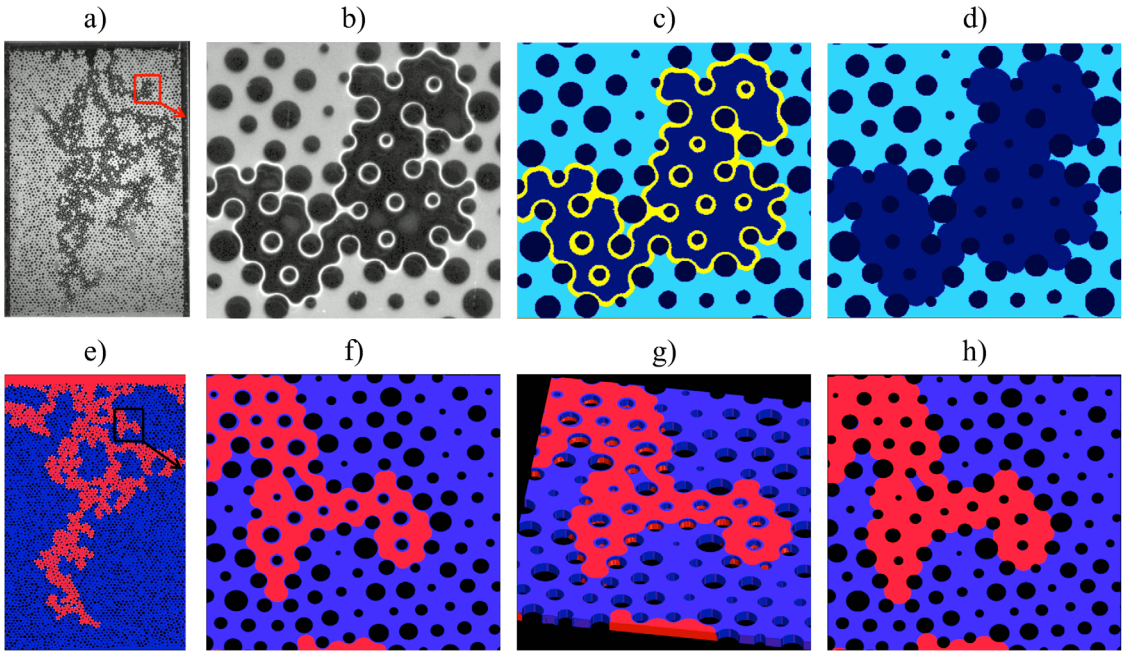

Figure 6. Example of the steps performed to calculate the interfacial length, including the wetting film into the air phase, for the experiment (first row) and the corresponding 3-D simulation (second row). Through image analysis, the wetting film around the obstacles (a, b) is selected, (c) isolated from the rest, and finally (d) included into the air. In the simulations, instead of considering (e–g) the distribution of the phases on the front plane, the same information is available by simply interpolate the color function on the midplane of medium, where (h) the air phase touches the obstacles.

by A_{sim} the analogous quantity for the image obtained from the simulation. The relative difference in air saturation between experimental and numerical images is

$$E_S = \frac{\sum_{i,j}\left(A_{exp}^{(i,j)} - A_{sim}^{(i,j)}\right)}{\sum_{i,j} A_{exp}^{(i,j)}}, \tag{13}$$

which gives a measure of the relative cell-saturation difference at breakthrough.

A better measure of the discrepancy between the displacement structures is the *mismatch ratio*,

$$\frac{E_{mm} = \sum_{i,j} |A_{exp}^{(i,j)} - A_{sim}^{(i,j)}|}{\sum_{i,j}\left(A_{exp}^{(i,j)} + A_{sim}^{(i,j)}\right)}, \tag{14}$$

which is in effect the sum of the nonoverlapping areas normalized by the sum of the total experimental and numerical areas. Notice that this normalization ensures that the error is one if there is no overlap between experiment and simulation. In this case the different regions invaded in the experiment but not invaded in the simulation and vice versa do not compensate each other and both contribute to E_{mm}. Saturation errors and *mismatch ratio*, calculated at breakthrough through equations (13) and (14), respectively, are shown in Table 2.

5. Discussion

5.1. Shape of the Invasion Structures

The geometry of observed displacement structures is typical of viscous-unstable flow dictated by an unfavorable viscosity ratio, and by a sufficiently high flow velocity. In the limiting case of an inviscid invading fluid, the pressure drop in the invasion structure is negligible and the pressure can be assumed constant. Except for capillary fluctuations, the pressure in the wetting fluid close to the interface is also constant, and

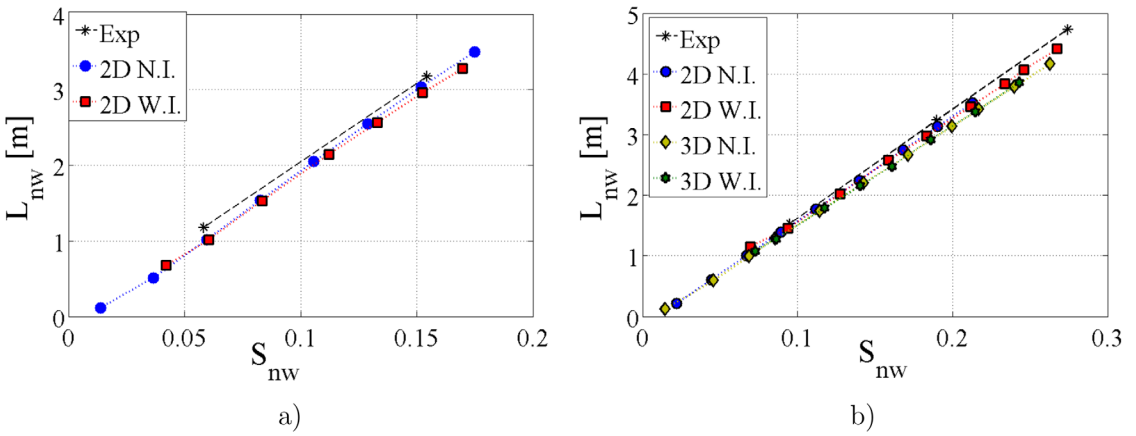

Figure 7. Interfacial length as a function of the nonwetting fluid saturation for (a) the homogeneous geometry and (b) the heterogeneous geometry (Exp = experiments; N.I. = simulations with no initialization; and W.I. = simulation with initialization).

the pressure is uniform over the outlet boundary of the medium as well. Hence, a small positive perturbation of the invading front (advancing ahead of the rest) increases the pressure gradient in the wetting fluid between the tip of the perturbation and the outlet, with respect to the unperturbed interface. This promotes the growth of the perturbation and the formation of fingers. Here, in contrast to the classical

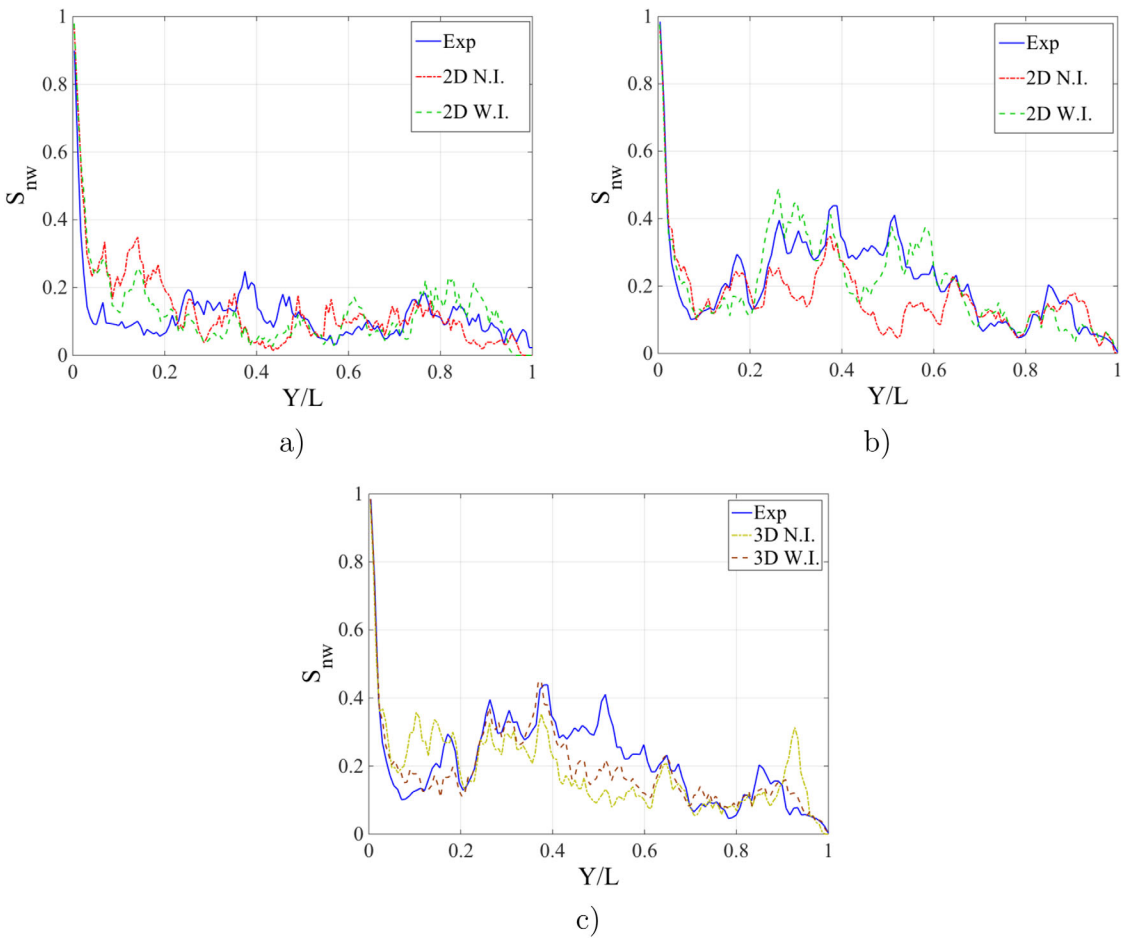

Figure 8. Average longitudinal saturation profile for (a) the homogeneous geometry; (b) the heterogeneous geometry and corresponding 2-D model; and (c) the heterogeneous geometry and 3-D model (Exp = experiments; N.I. = simulations with no initialization; and W.I. = simulation with initialization).

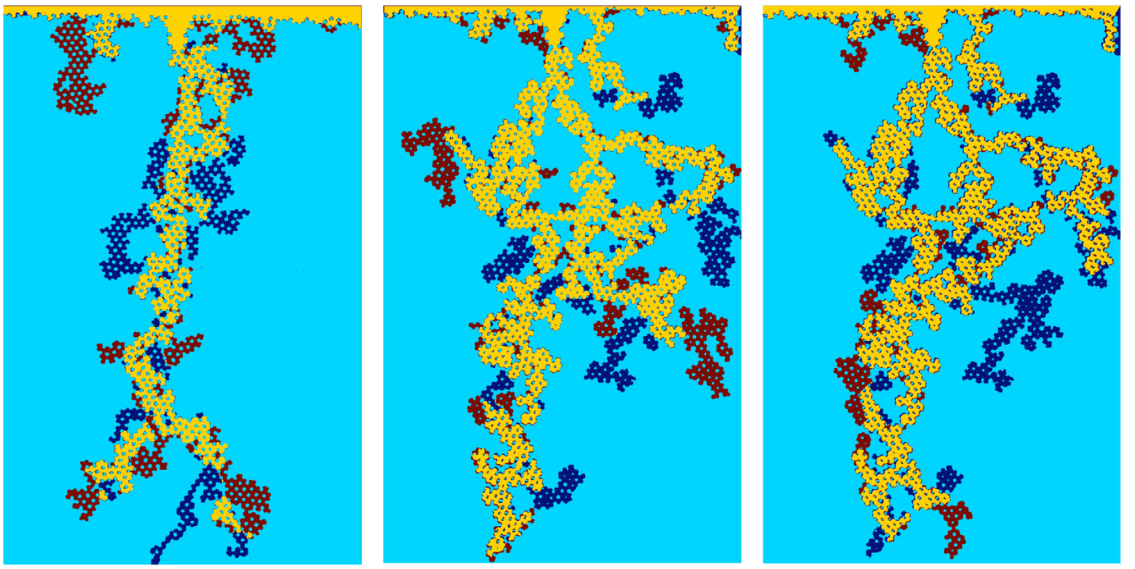

Figure 9. Experiments and simulations with initialization superimposed on the same image. Yellow represents the area that has been invaded in both experiments and numerical simulations; blue represents the area that has been invaded in the experiment but not in the simulations and red represents the area invaded in the simulations but not in the experiments. (a) Homogeneous geometry; (b) heterogeneous geometry, 2-D model; and (c) heterogeneous geometry, 3-D model.

Saffman-Taylor instability, in which the surface tension acts at the scale of the horizontal curvature radius, the presence of the grains generates capillary forces that act at the scale of the pore necks, which produces a rough interface with a different finger morphology. The pressure and the velocity fields leading to this complex invading structure cannot be observed in the experiments, but can be easily visualized from the numerical simulations, revealing very different velocity patterns in the two phases and a smaller but not negligible pressure drop in the air (Figure 10).

The qualitative differences between the invading structures observed in the two micromodels (Figure 3a) are explained by the local effects of the capillary forces. The distribution of pore throats results in a capillary pressure threshold distribution [*Løvoll et al*., 2004], which represents the distribution of the minimum entry pressures needed to invade each pore (see Figure 2b). Since the higher pore size variability of the heterogeneous geometry corresponds to a wider distribution of the capillary pressure thresholds, these fluctuations are more likely to prevail over the viscous pressure drop between pores that are not too far and produce a more ramified structure at a smaller scale. The different structures observed in the homogeneous and heterogeneous experiments demonstrate that even small differences in the width of the capillary pressure threshold distribution affect the local fluid distribution in the medium (here, the difference between the largest and the smallest pore in the heterogeneous geometry is less than 1 order of magnitude). The relative impact of the capillary threshold fluctuations, with respect to the viscous pressure drop, is quantified by the fluctuation number, F, defined in section 3.3.

5.2. Capability of the Simulations to Reproduce Experimental Displacement Patterns

The typical finger width is a critical feature to characterize the displacement structure: it corresponds to the spatial scale over which viscous forces dominate fluctuations in capillary pressure thresholds. Another important geometrical feature that has been extensively used in the literature is the fractal dimension, whose value is known for fingering regimes at small and large capillary numbers. The values obtained in the simulations for these two observables are in excellent agreement with the values measured from the experimental data. This demonstrates that the numerical model is able to properly capture the relevant pore-scale physical mechanisms that characterize the drainage process.

The temporal evolution of the interfacial length shows similar trends when comparing the simulations with the corresponding experiments (see Figure 7). Differences are observed only at breakthrough, which corresponds to the last point of the curve. In the homogeneous geometry, breakthrough occurs at later times in

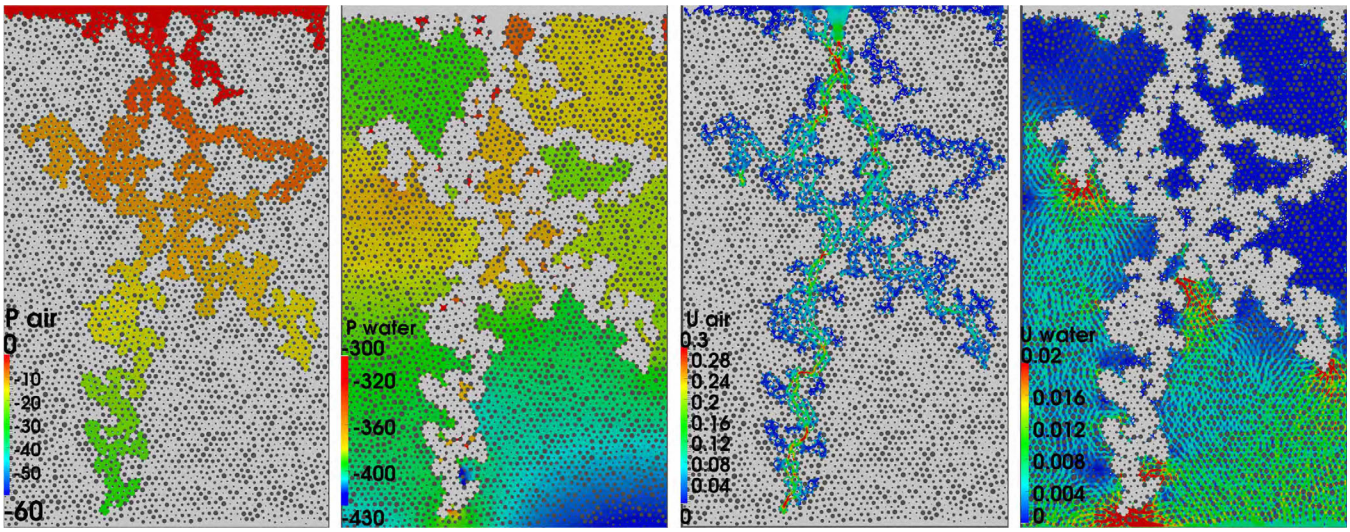

Figure 10. Pressure (Pa) and velocity fields (m/s) at breakthrough obtained for the heterogenous geometry using the 2D model. (a) Pressure field in the air phase (the water phase is white); (b) pressure field in the water phase (the air phase is white); (c) velocity field in the air phase (the water phase is white); and (d) velocity field in the water phase (the air phase is white).

the simulations and the interfacial length at breakthrough is overestimated by +10% if the finger is not initialized, and by +3% if the finger is initialized. On the contrary, in the simulations performed in the heterogeneous geometry, breakthrough occurs earlier compared to the experiment and the interfacial length is underestimated by −22% and −6% in case of 2-D simulations with and without initialization, respectively. When the 3-D model is employed, differences are reduced to approximately −15%, with very small changes depending on the initialization. Similar discrepancies are observed for the saturation errors at breakthrough (E_S, see Table 2).

The average saturation profiles display relatively large fluctuations due the limited lateral extension of the micromodels, which is not sufficient to provide a good statistics of the largest features of the displacement structure. In general, there is a good agreement between simulations and experiments in terms of the observed fluctuations (Figure 8).

The discrepancies between simulations and experiments are due to small differences in the displacement structures, which are well visible when the invasion structures are superimposed (Figure 9). Some parts of the displacement structures are not correctly captured by the simulations, which leads to different breakthrough times. In the following paragraph, we discuss the origin of these discrepancies and how they depend on the geometry, on the simulation initialization and on the model employed (2-D-integrated or full 3-D).

5.3. Origin of the Discrepancies Between Measured and Simulated Invasion Structures

A deterministic reproduction of the experimental viscous fingering is impossible due to the unstable nature of the process and to small discrepancies between the numerical and experimental geometries. Even if the geometry used for simulations has been acquired directly from experimental images, uncertainties remain on the exact position, shape, and size of the grains. When measuring the geometry from 2-D experimental images, we do not allow for noncylindrical grain shapes (grains tend to be slightly conical, and their section can also deviate from the perfect disk) and we do not account for parallax errors in the images. Moreover, the procedure used to construct the computational grid (split-hexahedral cells are created by snapping and iteratively refining a background hex-mesh on the triangulated surface geometry) introduces further discrepancies between the numerical porous medium model and the real one, which are of the order of the typical cell size. Besides pure geometrical discrepancies, there are other sources of error such as the uncertainty on the fluids properties or the uniform contact angle boundary condition assigned on the obstacles. The latter is only an approximation, because the wettability of the micromodel is likely to be nonuniform due to imperfections in the manufacturing and changes over sequential usage.

The mismatch ratio is smaller for the heterogeneous geometry (ranging from 17 to 30%) than for the homogeneous geometry (from 30 to 40%). This is due to the larger pore size variability of the heterogeneous

geometry, which limits the impact of the small discrepancies between the real geometry and the geometry used in the simulations. Indeed, these discrepancies can be regarded as small differences between the grain radii distributions, which affect the capillary pressure threshold distributions. We assume that the uncertainty on the real geometry is dominated by the finite resolution of the micromodel image that has been used to calculate the position of the grains and their radii. The error is then of the order of one pixel size, i.e., of $\delta r = 0.04$ mm. An error with the same order of magnitude is introduced during the mesh generation. If we also assume that the errors introduced by measuring the geometry from an experimental image and the inaccuracies associated with the gridding procedure are similar for both geometries, the probability that pore-to-pore variations in capillary thresholds dominate the pore-by-pore discrepancies in capillary threshold between the experimental geometry and the numerical one is larger in the heterogeneous geometry. In fact, the estimated error is about one standard deviation of the grain size distribution in the homogeneous geometry and about 0.3 standard deviations of that distribution in the heterogeneous geometry. In terms of capillary threshold distribution, it corresponds to a relative uncertainty on the capillary thresholds of $\delta r/\langle r \rangle = 8.3\%$, where $\langle r \rangle$ is the mean grain radius.

For similar reasons, a better agreement between numerical simulations and experiments is observed when the finger is initialized. Indeed, when the fluid distribution is initialized from an experimental image in which the finger has already started to develop, contrasts in viscous forces are significant along the developing finger, while there are no such contrasts along the initial interface, which has no roughness above the pore scale. Consequently, when the viscous instability has developed into a finite perturbation, the effects of the discrepancies between the numerical and the real geometry, which are of capillary origin, are more easily dominated by viscous effects. In particular, we then observe a suppression of the secondary fingers close to the inlet, as visible in Figures 3b–3e and 8a–8c.

Finally, the question of the comparison between experiments and simulations necessarily raises the question of the reproducibility of the experiments. When performing the same primary drainage experiment in a given geometry several times and under identical boundary conditions, we observe a small variability in the geometry of the interface at its entrance in the porous medium. As infinitesimal perturbations grow with time due to the unstable nature of the flow, that variability yields slightly different displacement structures, and this all the more as the pore space heterogeneity is smaller. In this respect, the experimental data (not shown here) indicates a mismatch ratio E_{mm} of about 10% between successive experiments performed in the same homogeneous micromodel. The small variability in the initial conditions for the growth of fingers, which is the main cause for that mismatch, also explains the impact of finger initialization in the simulations, discussed above. This is also why the difference in mismatch ratio between simulations performed with or without initialization is expected to be of the same order as the one observed between experiments performed under identical conditions. These mismatch ratios are indeed of the same order (see Table 2); for geometries yielding perfectly reproducible experiments, we would observe little difference between simulations performed with and without initialization.

In conclusion, the mismatch ratio between the numerical and experimental displacement structures can be attributed to the uncertainty on the geometry, to the assumption of uniform wettability, and to slightly different initial conditions at the entrance of the porous medium.

5.4. Accuracy of the 2-D and 3-D Models

In general, good results are obtained both with the 2-D and the 3-D models. When the finger is not initialized, a slightly better match with the experiment is obtained when the 3-D model is employed. However, by comparing the results of 2-D and 3-D simulations with initialization, we observe that the 2-D simulation performs slightly better in terms of the error indicators reported in Table 2 (in particular, the saturation error at breakthrough is almost exact). The reason that the 3-D model is not more accurate than the 2-D model might be purely a hazard of the statistics, and the relative performance of the two models might change under different experimental conditions or in different geometries. Furthermore, wetting films in the corners are explicitly described in the 3-D simulation. If the geometry used in the simulations were identical to the real geometry, this would help to faithfully describe the pore invasion, which is influenced by the effects of the film on the pore entry pressure. However, the effects of small discrepancies between the experimental and the numerical geometries might dominate. In addition, the finger initialization of the 3-D model from a 2-D experimental image might be not accurate enough, as no information about the fluid

distribution in the third-dimension is available. Another limit to the accuracy of the 3-D model is the discretization of the vertical direction. We have shown [*Ferrari and Lunati*, 2013] that a discretization of 15 cells per obstacle is enough to ensure that the difference to the results obtained with a finer grid be below 5%. However, the grid-convergence test was performed for 2-D geometries and the resolution required to accurately capture complex 3-D effects might be larger. In any case, our results suggest that, given the remaining uncertainty on the real geometry (and the limited numerical resolution), the simulation of unstable drainage in quasi-2-D micromodels is not considerably improved by an explicit description of the third-dimension.

6. Conclusions

We have presented a detailed analysis of unstable primary drainage experiments in micromodels that have been manufactured by soft lithography and consist of quasi two-dimensional porous media (Hele-Shaw cell, containing cylindrical obstacles), two degrees of heterogeneity in the grain size distribution. The experiments have been modeled by means of Navier-Stokes simulations in which mass and momentum conservation equations are solved to obtain pressure and velocity distributions in the pore space. The Navier-Stokes solver is coupled with the Volume of Fluid (VOF) method, which tracks the evolution of the interface between the two fluids, by solving a simple advection equation.

Modeling unstable flow regimes (such as the displacement of a more viscous fluid by a less viscous fluid that has been considered here) is a significant challenge because small errors are amplified and lead to inaccurate predictions at later times. We have demonstrated that even for an unstable flow regime the numerical model is able to predict the invasion structure reasonably well. A pore-by-pore comparison shows that a large part of the invasion structure is predicted correctly. For a more heterogeneous geometry, up to more than 80% of the invasion structure is captured in the simulation, whereas in the less heterogeneous geometry the fraction that is correctly captured can reach 70%.

The remaining differences between simulations and experiments result from uncertainties on the exact geometry and on fluid properties, from the fact that the initial perturbation cannot be known with an arbitrarily large precision, and from discretization errors; the joint impact of this lack of information is enhanced by the unstable nature of the flow. Simulations in a more heterogeneous geometry lead to a better local match with the experiments because the large, measurable pore-to-pore variations dominate pore-by-pore discrepancies between the experimental geometry and the numerical geometry. On the contrary, simulating drainage in a weakly heterogeneous geometry is more challenging because the uncertainties on the real dimensions of the pore necks may be of the same order of magnitude as the pore-to-pore variability of pore necks in the medium.

In most applications, the geometry of the porous medium is never known exactly and a statistical description is used both for the geometry and the resulting fluid structures. Therefore, the numerical model should be able to correctly reproduce the main statistical properties of the process. We have shown that the numerical model is indeed able to provide an excellent estimate of the most important statistical indicators (e.g., typical width of air fingers, fractal dimension of the air pattern, air-water interfacial length, air saturation at breakthrough, and average longitudinal air saturation profile).

Even with the relatively coarse discretization required to balance accuracy and computational costs, our results demonstrate that both 2-D integrated and 3-D models are able to accurately model the pore-scale processes occurring during unstable displacement in micromodels. The numerical model is reliable and can be used to complement experimental observations with information on quantities that are difficult to measure or that are not at all accessible in the laboratory. An example is the velocity field (see Figure 10), which is of paramount importance to understand how transport and mixing of a solute occur within each fluid phase during the displacement process.

Acknowledgments

A.F. and I.L. are supported by the Swiss National Science Foundation grants PP00P2–123419/1 and PP00P2–144922/1. J.J.-M. expresses his gratitude to Fondation Rennes 1 (Chaire Environment et Innovation) and acknowledges support from Université Rennes 1 for travel between Rennes and Lausanne. Y.M. and T.L.-B. gratefully acknowledge support from Fondation Herbette for the same purpose. Y.M. also acknowledges support from Rennes-Métropole through an A.I.S. grant for equipment and from CNRS/INSU under grant 786971 of the EC2CO program. The authors commit to making their data available to any reader who requires it.

References

Afkhami, S., S. Zaleski, and M. Bussmann (2009), A mesh-dependent model for applying dynamic contact angles to VOF simulations, *J. Comput. Phys.*, *228*(15), 5370–5389.

Aker, E., K. J. Måløy, A. Hansen, and G. G. Batrouni (1998), A two-dimensional network simulator for two-phase flow in porous media, *Transp. Porous Media*, *32*, 163–186.

Aker, E., K. J. Måløy, and A. Hansen (2000a), Viscous stabilization of 2D drainage displacements with trapping, *Phys. Rev. Lett.*, *84*, 4589–4592.
Aker, E., K. J. Måløy, and A. Hansen (2000b), Burst dynamics during drainage displacements in porous media: Simulations and experiments, *Europhys. Lett.*, *51*(1), 55–61.
Bandara, U. C., A. M. Tartakovsky, and B. J. Palmer (2011), Pore-scale study of capillary trapping mechanism during CO_2 injection in geological formations, *Int. J. Greenhouse Gas Control*, *5*(6), 1566–1577.
Bandara, U. C., A. Tartakovsky, M. Oostrom, B. Palmer, J. Grate, and C. Zhang (2013), Smoothed particle hydrodynamics pore-scale simulations of unstable immiscible flow in porous media, *Adv. Water Resour.*, *62*, 356–369.
Bear, J. (1972), *Dynamics of Fluids in Porous Media*, 764 p., Elsevier, N. Y.
Berberović, E., N. P. van Hinsberg, S. Jakirlić, I. V. Roisman, and C. Tropea (2009), Drop impact onto a liquid layer of finite thickness: Dynamics of the cavity evolution, *Phys. Rev. E*, *79*, 036306.
Blunt, M. J., M. D. Jackson, M. Piri, and P. H. Valvatne (2002), Detailed physics, predictive capabilities and macroscopic consequences for pore-network models of multiphase flow, *Adv. Water Resour.*, *25*(8), 1069–1089.
Blunt, M. J., B. Bijeljic, H. Dong, O. Gharbi, S. Iglauer, P. Mostaghimi, A. Paluszny, and C. Pentland (2013), Pore-scale imaging and modelling, *Adv. Water Resour.*, *51*, 197–216.
Brackbill, J., D. B. Kothe, and C. Zemach (1992), A continuum method for modeling surface tension, *J. Comput. Phys.*, *100*(2), 335–354.
Chen, Q., and W. Kinzelbach (2002), An NMR study of single-and two-phase flow in fault gouge filled fractures, *J. Hydrol.*, *259*(1), 236–245.
Chen, Q., W. Kinzelbach, and S. Oswald (2002), Nuclear magnetic resonance imaging for studies of flow and transport in porous media, *J. Environ. Qual.*, *31*(2), 477–486.
de Anna, P., J. Jimenez-Martinez, H. Tabuteau, R. Turuban, T. Le Borgne, M. Derrien, and Y. Méheust (2014), Mixing and reaction kinetics in porous media: An experimental pore scale quantification, *Environ. Sci. Technol.*, *48*(1), 508–516.
Fatt, I. (1956), The network model of porous media, *Trans. Am. Inst. Min. Metall. Pet. Eng.*, *207*, 144–181.
Ferrari, A., and I. Lunati (2013), Direct numerical simulations of interface dynamics to link capillary pressure and total surface energy, *Adv. Water Resour.*, *57*, 19–31.
Ferrari, A., and I. Lunati (2014), Inertial effects during irreversible meniscus reconfiguration in angular pores, *Adv. Water Resour.*, *74*, 1–13.
Gomaa, H., S. Kumar, C. Huber, B. Weigand, and B. Peters (2011), Numerical comparison of 3D jet breakup using a compression scheme and an interface reconstruction based VOF-code, in *24th European Conference on Liquid Atomization and Spray Systems*, Estoril, Portugal.
He, X., and L.-S. Luo (1997), Lattice Boltzmann model for the incompressible Navier–Stokes equation, *J. Stat. Phys.*, *88*(3–4), 927–944.
Hele-Shaw, H. (1898), Flow of water, *Nature 58*(1489), pp. 34–36.
Hirt, C. W., and B. D. Nichols (1981), Volume of fluid (VOF) method for the dynamics of free boundaries, *J. Comput. Phys.*, *39*(1), 201–225.
Horgue, P., F. Augier, M. Quintard, and M. Prat (2012), A suitable parameterization to simulate slug flows with the volume-of-fluid method, *C. R. Méc.*, *340*(6), 411–419.
Horgue, P., F. Augier, P. Duru, M. Prat, and M. Quintard (2013), Experimental and numerical study of two-phase flows in arrays of cylinders, *Chem. Eng. Sci.*, *102*, 335–345.
Joekar Niasar, V., S. Hassanizadeh, L. Pyrak-Nolte, and C. Berentsen (2009), Simulating drainage and imbibition experiments in a high-porosity micromodel using an unstructured pore network model, *Water Resour. Res.*, *45*, W02430, doi:10.1029/2007WR006641.
Kang, Q., P. C. Lichtner, and D. Zhang (2007), An improved lattice Boltzmann model for multicomponent reactive transport in porous media at the pore scale, *Water Resour. Res.*, *43*, W12S14, doi:10.1029/2006WR005551.
Lenormand, R., and C. Zarcone (1985), Invasion percolation in an etched network: Measurement of a fractal dimension, *Phys. Rev. Lett.*, *54*(20), 2226–2229.
Lenormand, R., E. Touboul, and C. Zarcone (1988), Numerical models and experiments on immiscible displacement in porous media, *J. Fluid Mech.*, *189*, 165–187.
Lerdahl, T. R., P.-E. Oren, and S. Bakke (2000), A Predictive Network Model for Three-Phase Flow in Porous Media, Society of Petroleum Engineers, doi:10.2118/59311-MS.
Løvoll, G., Y. Méheust, R. Toussaint, J. Schmittbuhl, and K. J. Måløy (2004), Growth activity during fingering in a porous Hele-Shaw cell, *Phys. Rev. E*, *70*, 026301.
Lunati, I. (2007), Youngs law and the effects of interfacial energy on the pressure at the solid-fluid interface, *Phys. Fluids*, *19*(11), 118105.
Lunati, I., and D. Or (2009), Gravity-driven slug motion in capillary tubes, *Phys. Fluids*, *21*(5), 052003.
Måløy, K. J., J. Feder, and T. Jøssang (1985), Viscous fingering fractals in porous media, *Phys. Rev. Lett.*, *55*(24), 2688–2691.
Måløy, K. J., F. Boger, J. Feder, T. Jøssang, and P. Meakin (1987), Dynamics of viscous-fingering fractals in porous-media, *Phys. Rev. A*, *36*, 318–324.
Meakin, P., and A. M. Tartakovsky (2009), Modeling and simulation of pore-scale multiphase fluid flow and reactive transport in fractured and porous media, *Rev. Geophys.*, *47*, RG3002, doi:10.1029/2008RG000263.
Méheust, Y., G. Løvoll, K. J. Måløy, and J. Schmittbuhl (2002), Interface scaling in a two-dimensional porous medium under combined viscous, gravity and capillary effects, *Phys. Rev. E*, *66*, 051603.
Monaghan, J. J. (1994), Simulating free surface flows with SPH, *J. Comput. Phys.*, *110*(2), 399–406.
OpenFOAM (2011), *User Guide*, version 2.0.0, OpenCFD Ltd, U. K. [Available at www.openfoam.org.]
Porter, M. L., M. G. Schaap, and D. Wildenschild (2009), Lattice-Boltzmann simulations of the capillary pressure–saturation–interfacial area relationship for porous media, *Adv. Water Resour.*, *32*(11), 1632–1640.
Raeini, A. Q., M. J. Blunt, and B. Bijeljic (2014), Direct simulations of two-phase flow on micro-CT images of porous media and upscaling of pore-scale forces, *Adv. Water Resour.*, *74*, 116–126.
Rusche, H. (2003), Computational fluid dynamics of dispersed two-phase flows at high phase fractions, PhD thesis, Imp. Coll. London, London, U. K.
Saffman, P. G., and G. Taylor (1958), The penetration of a fluid into a porous medium or Hele-Shaw cell containing a more viscous liquid, *Proc. R. Soc. London, Ser. A*, *245*, 312–329.
Scardovelli, R., and S. Zaleski (1999), Direct numerical simulation of free-surface and interfacial flow, *Ann. Rev. Fluid Mech.*, *31*(1), 567–603.
Schaap, M. G., M. L. Porter, B. S. Christensen, and D. Wildenschild (2007), Comparison of pressure-saturation characteristics derived from computed tomography and lattice Boltzmann simulations, *Water Resour. Res.*, *43*, W12S06, doi:10.1029/2006WR005730.
Shan, X., and H. Chen (1993), Lattice Boltzmann model for simulating flows with multiple phases and components, *Phys. Rev. E*, *47*(3), 1815–1819.
Tartakovsky, A., and P. Meakin (2005), Modeling of surface tension and contact angles with smoothed particle hydrodynamics, *Phys. Rev. E*, *72*(2), 026301.

Tomin, P., and I. Lunati (2013), Hybrid multiscale finite volume method for two-phase flow in porous media, *J. Comput. Phys.*, *250*, 293–307.
Toussaint, R., G. Løvoll, Y. Méheust, J. Schmittbuhl, and K. J. Måløy (2005), Influence of pore-scale disorder on viscous fingering during drainage, *Europhys. Lett.*, *71*(4), 583–589.
Toussaint, R., K. J. Måløy, Y. Méheust, G. Løvoll, M. Jankov, G. Schäfer, and J. Schmittbuhl (2012), Two-phase flow: Structure, upscaling, and consequences for macroscopic transport properties, *Vadose Zone J.*, *11*(3).
Vinningland, J. L., Ø. Johnsen, E. G. Flekkøy, R. Toussaint, and K. J. Måløy (2007), Experiments and simulations of a gravitational granular flow instability, *Phys. Rev. E*, *76*(5), 051306.
Vogel, H.-J., J. Tölke, V. Schulz, M. Krafczyk, and K. Roth (2005), Comparison of a lattice-Boltzmann model, a full-morphology model, and a pore network model for determining capillary pressure–saturation relationships, *Vadose Zone J.*, *4*(2), 380–388.
Wägli, P., A. Homsy, and N. de Rooij (2011), Norland optical adhesive (NOA81) microchannels with adjustable wetting behavior and high chemical resistance against a range of mid-infrared-transparent organic solvents, *Sens. Actuators B Chem.*, *156*(2), 994–1001.
Wildenschild, D., and A. P. Sheppard (2013), X-ray imaging and analysis techniques for quantifying pore-scale structure and processes in subsurface porous medium systems, *Adv. Water Resour.*, *51*, 217–246.
Xia, Y., and G. M. Whitesides (1998), Soft lithography, *Ann. Rev. Mater. Sci.*, *28*(1), 153–184.
Yang, X., T. D. Scheibe, M. C. Richmond, W. A. Perkins, S. J. Vogt, S. L. Codd, J. D. Seymour, and M. I. McKinley (2013), Direct numerical simulation of pore-scale flow in a bead pack: Comparison with magnetic resonance imaging observations, *Adv. Water Resour.*, *54*, 228–241.